

The Meyer–Neldel rule in amorphous TiO₂ films with different Fe content

Diana Mardare^{a)}

Department of Physics, “Alexandru Ioan Cuza” University, Faculty of Physics, 700506-Iasi, Romania

Abdullah Yildiz

Department of Energy Systems Engineering, Faculty of Engineering and Natural Sciences, Yıldırım Beyazıt University, 06030, Ankara, Turkey

Radu Apetrei, Petronela Rambu, and Daniel Florea

“Alexandru Ioan Cuza” University, Faculty of Physics, 700506-Iasi, Romania

Nicoleta Georgiana Gheorghe, Dan Macovei, and Cristian Mihail Teodorescu

National Institute of Materials Physics, 077125-Magurele-Ilfov, Romania

Dumitru Luca

“Alexandru Ioan Cuza” University, Faculty of Physics, 700506-Iasi, Romania

(Received 15 February 2012; accepted 30 May 2012)

Amorphous titania thin films with increasing Fe content have been prepared by RF magnetron sputtering. X-ray absorption spectroscopy revealed modifications of both local structures/environment of the Ti and Fe atoms, with formation of phases containing amorphous material and a magnetite-like phase. The temperature dependence of the electrical conductivity of the films was investigated for temperatures higher than half of the Debye temperature ($T > 391$ K). It was found that the electrical conductivity in the amorphous Fe/TiO₂ films obeys the Meyer–Neldel rule. The origin of this behavior is explained on the basis of the multiphonon-assisted hopping model.

I. INTRODUCTION

Titanium dioxide (TiO₂), a nontoxic and a low-cost material, has received significant attention of materials scientists, being extensively investigated (especially as thin films) for its unique physical and chemical properties (high oxidation power, high optical transmittance in the visible range, high refractive index, good mechanical and chemical stability in adverse environments, etc.). These remarkable properties, which make it suitable for a variety of applications (photodegradation, gas sensors, solar cells, self-cleaning, etc.^{1–5}), can be further improved by doping titania materials with various impurities. Since Matsumoto et al.⁶ have discovered room-temperature ferromagnetism in Co-doped TiO₂ films, many attempts have been made to dope TiO₂ with transition metals. Among various dopants (Cr, Mn, Fe, Co), iron atom is the most favorable substituent for titanium in the TiO₂ lattice, due to close values of Fe³⁺ and Ti⁴⁺ ion radii.⁷ Therefore, it is known for long that Fe/TiO₂ thin films exhibit room-temperature ferromagnetism.⁸ As for the controversial role of Fe dopant in enhancing the photocatalytic activity of the TiO₂ films, we have established the beneficial role of Fe³⁺ impurities

in the electron–hole separation processes⁹ for the case of low dopant concentration (1–3 at.%).

Extended x-ray absorption fine structure (EXAFS) and x-ray absorption near-edge structure (XANES) are non-destructive techniques for studying the local structure around a selected element contained in a material and the chemical environment, respectively. We have used it to derive information on the local environment around impurity atoms introduced in the matrix host¹⁰ by monitoring the absorption spectrum of the material in a synchrotron facility upon gradually increasing the energy of the incident x-ray photons. Actually, we focus in the current paper on the structural, elemental, and electrical characterization of TiO₂ thin films with increasing Fe content, concentrating on the local structure around iron atoms, with the aim to explain the mechanism of the electrical conduction in these thin films.

II. EXPERIMENTAL DETAILS

Titania thin films with increasing iron content have been prepared by RF magnetron sputtering (13.56 MHz) on microscope glass substrates heated at 300 °C, placed at 6 cm in front of the target, in a 30-L deposition chamber (base pressure 1.5×10^{-5} mbar). A mosaic target arrangement has been used with 1–3 sintered Fe₂O₃ disks (3.5 mm in diameter) placed on the ceramic TiO₂ target (76.2 mm in diameter) in the high-rate sputtering area of the target. The Fe/TiO₂ thin films were accordingly denoted

^{a)}Address all correspondence to this author.

e-mail: dianam@uaic.ro

DOI: 10.1557/jmr.2012.193

as Sample 1/3, Sample 2/3, and Sample 3/3. A reference sample was also prepared with no iron content in it, under the same experimental conditions. Argon at 7×10^{-3} mbar was used as the sputtering gas.

The crystalline structure of the films was studied with a Bruker D8 Advantage diffractometer (Bruker AXS Inc., Madison, WI; CuK α radiation, $\lambda = 1.540591$ Å) at 4° grazing incidence angle of the incident beam with respect to film surface.

Survey and narrow-scan x-ray photoelectron spectroscopy (XPS) spectra were recorded to derive the elemental composition and chemical state in the films' surface region by using a Physical Electronics-ULVAC (PHI 5000 VersaProbe, ULVAC-PHI, Inc., Kanawaga, Japan) XPS instrument. A monochromatic AlK α x-ray radiation ($h\nu = 1486.7$ eV) was used as excitation source and a take-off photoelectron angle of 45°.

The XANES and the EXAFS measurements were performed in the fluorescence mode at the Doris storage ring facility in the Hasylab synchrotron facility in Hamburg, Germany. The measurements were made using the beam-line E4 (EXAFS II) of this research facility using a double crystal Si(111) monochromator, preceded by a focusing mirror for intensity enhancement. Ti and Fe K-edge spectra were measured in K α -fluorescence yield mode, using a 7-pixel Si(Li) detector. As reference samples, metal foils of Fe and Ti or Fe₂O₃, Fe₃O₄, TiO₂, and TiO powders (pressed in pellets) were used.

To perform electrical conductivity versus temperature measurements, two parallel thin-film Ag electrodes (0.8 mm spacing) have been grown by thermal evaporation on top of films surfaces. These measurements have been done during two heating and cooling cycles between 391 and 500 K.

III. RESULTS AND DISCUSSION

All the as-deposited Fe/TiO₂ films are amorphous, as confirmed by the x-ray diffraction data.

The deconvolution of the narrow-scan XPS spectra showed that the Fe/Ti atomic ratios in Sample 1/3 to 2/3 to 3/3 increased in the sequence 0.3 to 0.5 to 0.8, respectively. All the as-prepared samples, including the reference one, are oxygen deficient since sample deposition has been done in an oxygen-free atmosphere, thus favoring the occurrence of oxygen vacancies in the films.¹¹ The high-resolution XPS spectrum of the O 1s peak shows a "surface" component at a binding energy (BE) of 533.3 eV and second component related to the oxygen bound to Ti, at BE = 532.5 eV.

Figures. 1 and 2 present the Ti 2p and the Fe 2p XPS spectra of the investigated films, respectively.

The peak analysis of the Ti 2p_{3/2} XPS spectra indicated a main Ti⁴⁺ component and gradually less significant amount of Ti³⁺ and Ti²⁺ species. The ratio of the Ti³⁺/Ti⁴⁺ components peak area decrease monotonically upon increas-

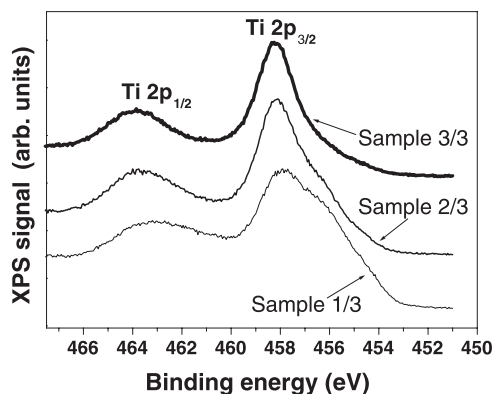


FIG. 1. The Ti 2p XPS spectra of the investigated films.

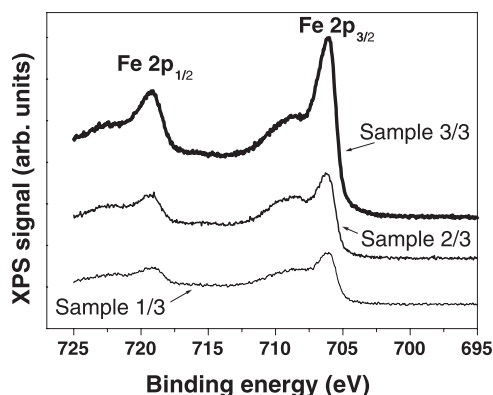


FIG. 2. The Fe 2p XPS spectra of the investigated films.

ing the Fe content in the samples from 0.4 (Sample 1/3) to 0.3 (Sample 2/3) to 0.1 (Sample 3/3), while the ratio of the Ti²⁺/Ti⁴⁺ components peak area decrease from 0.7 to 0.2 to 0.1 for the corresponding samples.

The Fe 2p_{3/2} XPS peak contained three components: (i) one corresponding to nonreacted iron (Fe⁰), weighting about 25% from to the total amount of Fe in the Sample 1/3 and 20% in the Sample 3/3; (ii) a Fe²⁺ component weighting constantly about 15% in all samples; and (iii) the main Fe³⁺ component accounts for the balance. The O/Ti atomic ratio in the reference sample is 1.8, while the O/(Ti + Fe) concentration ratio decreased from 1.2 to 1.1 to 0.8 upon increasing the Fe content in the samples.

The Ti K-edge XANES (Fig. 3) exhibits from the very beginning a noticeable difference with respect to the corresponding spectrum of pure anatase. The insert in Fig. 3 presents the preedge region of the XANES spectra, which is normally attributed to a mixture of 1s → 3d quadrupole transitions (at lower energies) and dipole transitions from 1s to 4p states hybridated with the 3d states in noncentrosymmetric phases (at higher energies).^{12–15} The film analyzed (Sample 3/3) seems to present only the quadrupole transition, thus evolution toward placement in centrosymmetric sites of Ti atoms is highly possible. A similar effect was reported in xerogel Fe-doped titania.¹⁶

The Fe K-edge XANES (Fig. 4), on contrary, presents features quite similar to that of iron oxides (hematite α -Fe₂O₃ and magnetite Fe₃O₄). However, the small preedge peak of common iron oxides is almost completely quenched in the case of Fe–Ti oxide samples. Though no systematic investigation of the preedge peak in Fe K-edge XANES has been reported, as in the case of titanium compounds, this decrease suggests a similar behavior of the Fe 3*d* states as that of Ti 3*d*, namely a weaker hybridization with the 4*p* states.

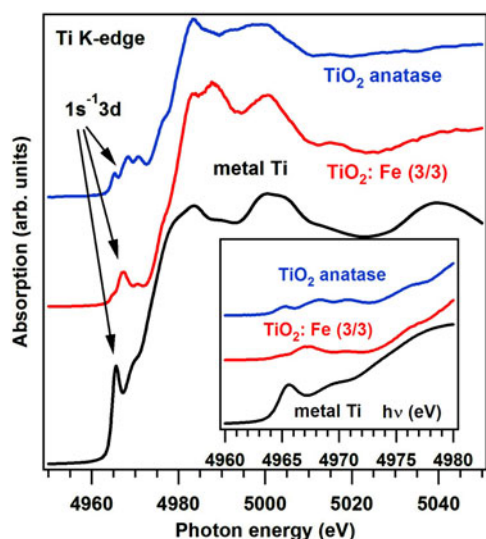


FIG. 3. Ti K-edge XANES spectra of anatase TiO₂, the sample with the largest Fe content (3/3), and metal Ti. The insert presents a zoom of the preedge region.

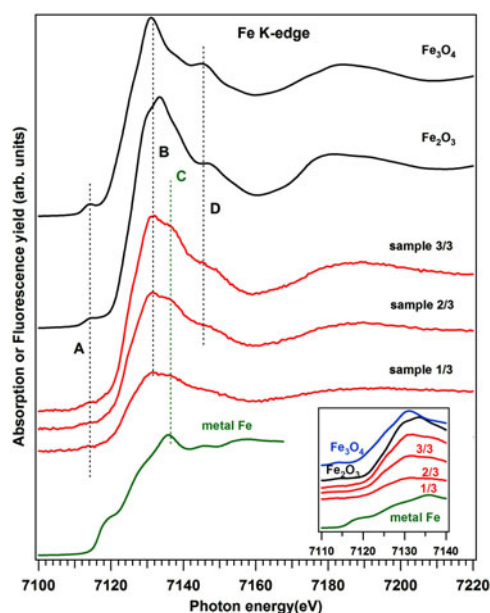


FIG. 4. Fe K-edge XANES spectra of Fe-doped titanium oxide, together with reference spectra of metal Fe and of α -Fe₂O₃ and Fe₃O₄. Insert: edge region.

Another remark is the absence of features related to both metal Fe and FeO in XANES.¹⁷ Since fluorescence detected XANES is much more bulk sensitive as compared with XPS owing to a considerably larger penetration/escape depth of x-rays (micrometers) as compared with the electron escape depth (nanometers), from this observation, one must conclude that Fe⁰ metal aggregates and Fe²⁺ compounds are agglomerated in the neighborhood of the film surface for all samples. This is probably connected also to the observed oxygen vacancies and to the presence of Ti³⁺. Actually, most oxide layers prepared by both magnetron sputtering and pulsed laser deposition exhibit oxygen depletion at the surface, going up to the stabilization of new phases.¹⁸ Consequently, the “true” Fe concentration in the bulk of all investigated layers may be recomputed from the XPS data as taking into account the Fe³⁺ concentration only. This yields 0.18, 0.32, and 0.52 for the ratio Fe/Ti for Samples 1/3, 2/3, and 2/3, respectively.

Figure 5 presents the results of the investigation of the EXAFS region at the Fe K-edge. In Fig. 5(a), the EXAFS functions are plotted. An increase of the local order around Fe atoms is quite visible as function on the Fe content (from Sample 1/3 to Sample 3/3). Actually, statistics did not allow a recording of suitable EXAFS spectrum for Sample 1/3, whereas for Sample 3/3, one can easily identify the occurrence of structures (8–9 Å⁻¹) typical of magnetite. Formation of metal (Fe) clusters is precluded from the EXAFS spectra. The Fourier transforms presented in Fig. 5(b) show, indeed, the increase of the ordering and formation of units close to bulk iron oxides with the increase of Fe content, shown by the progressive occurrence of large distance well-defined features. However, the low distance Fe–O peak remains the dominant one and this suggests the coexistence of two phases, an amorphous and a nanocrystalline one, with the latter close of Fe₃O₄ structures. Note also that the distance *R* from Fig. 5(b) is not the true interatomic distance; it has to be corrected by the appropriate EXAFS phase shifts, as those discussed in Ref. 19. Thus, the vertical lines are not “true” bond lengths but “apparent” ones, as derived from the EXAFS Fourier analysis. The amorphous phase is represented by a strong increase of the first Fe–O peak.

To investigate the charge transport mechanism in the amorphous Fe/TiO₂ films, the temperature dependence of the electrical conductivity (σ) was monitored during the variation of the temperature between 391 and 500 K. As shown in Fig. 6, a semiconductor-like increase of σ versus temperature is specific for the investigated materials. The electrical conductivity decreases significantly with the increasing Fe content. This could be explained by the decrease in the electron concentration since Fe impurities act as acceptor impurities.²⁰

In semiconductors, the main conduction mechanism is related to the excited carriers beyond the mobility edge

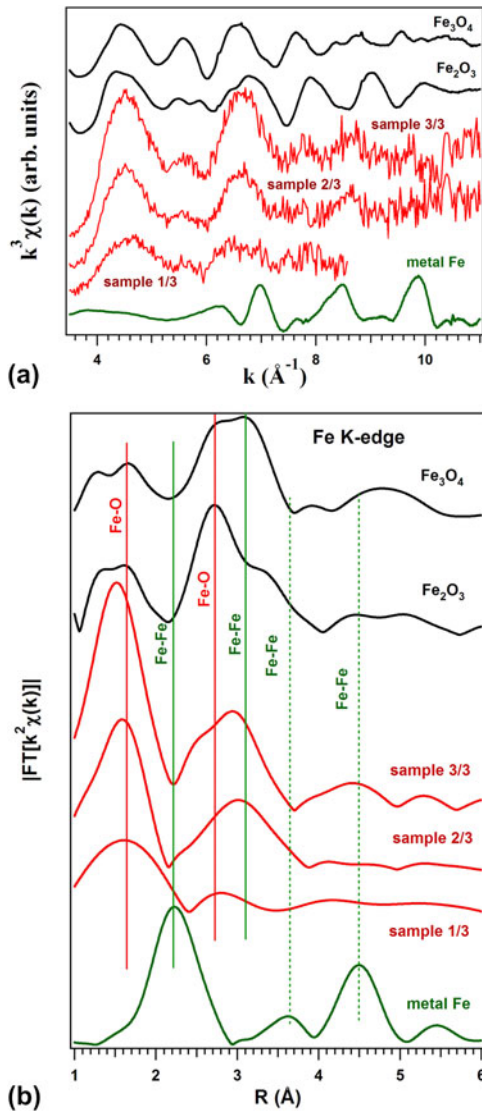


FIG. 5. (a) EXAFS functions $k^3\chi(k)$ recorded at the Fe K-edge, for the same samples as in Fig. 4. (b) The moduli of the Fourier transforms of the EXAFS spectra. Vertical lines denote typical Fe-neighboring apparent lengths.

into the nonlocalized or extended states, and the electrical conductivity is expressed by the Arrhenius relation:

$$\sigma = \sigma_0 \exp\left(-\frac{E_a}{k_B T}\right), \quad (1)$$

where σ_0 is a preexponential factor, E_a is thermal activation energy, and k_B is Boltzmann's constant.

To obtain a better insight in the charge transport in our samples, we should focus on the Arrhenius relation [Eq. (1)]. The values of E_a and σ_0 are calculated from the slopes and ordinate intercepts of the straight lines in Fig. 6. The magnitude of σ_0 in Eq. (1) depends on the sample nature and does not usually depend on E_a .²¹ There are, however, situations like the one first described by

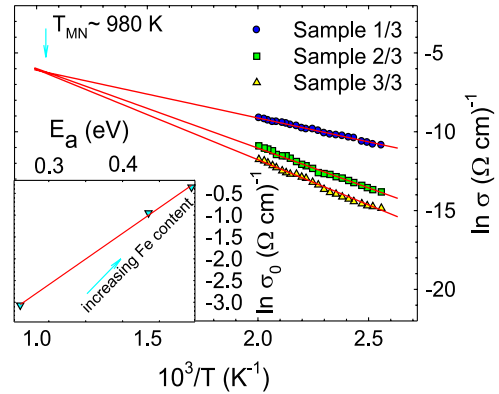


FIG. 6. Temperature dependence of the electrical conductivity plotted as $\ln(\sigma)$ versus $10^3/T$ for the studied samples. Solid lines are the best-fit lines with Eq. (1). The insert represents the relationship between the preexponential factor (σ_0) and the activation energy (E_a). Solid line is the best-fit line with Eq. (2).

Meyer and Neldel,²² where σ_0 varies with E_a . We have here such a situation (see the insert in Fig. 6), which is known as the Meyer–Neldel rule (MNR). One can easily notice that the activation energy increases upon increasing the Fe content in the films, fact related to the charge carrier depletion and the corresponding decrease of localized state density in the band gap.²⁰ The MNR has been observed in a wide range of materials including polycrystalline,²³ amorphous,²⁴ and organic materials.²⁵ This rule describes an exponential relation between σ_0 and E_a :

$$\sigma_0 = \sigma_{00} \exp\left(\frac{E_a}{E_{MN}}\right), \quad (2)$$

where σ_{00} and $1/E_{MN}$ are the MNR preexponential factor and MNR slope, respectively.²² In the insert presented in Fig. 6, the solid line indicates the best fit to the experimental data. It can be seen that our experimental data can be well described by the MNR. The estimated values of σ_{00} and E_{MN} from Eq. (2) are $2.17 \times 10^{-3} \Omega^{-1}/\text{cm}$ and 84.7 meV, respectively, which are typical values for a variety of disordered materials.²⁶

Substituting Eq. (2) into Eq. (1) yields:

$$\sigma = \sigma_{00} \exp\left[\left(\frac{1}{E_{MN}} - \frac{1}{k_B T}\right) E_a\right], \quad (3)$$

which gives a single crossing point for different activation energies at a temperature (T_{MN}) given by:

$$T_{MN} = \frac{E_{MN}}{k_B}. \quad (4)$$

It is clear that σ becomes independent of the activation energy at this temperature. T_{MN} can be estimated from Eq. (4) to be 983 K for our investigated samples.

Although several models have been proposed,^{27–29} the origin of the MNR is still unclear. The temperature dependence of the conductivity in the presence of the MNR seems more complicate. It is important to consider the values of σ_{00} and E_a to clearly distinguish which model is appropriate to describe the experimental data. It can be seen that the value of E_a is significantly large compared to $h\nu_0$ (ν_0 —the optical phonon frequency), which is of the order of the Debye energy. Recently, Han et al.³⁰ found a value of 781.6 K for the Debye temperature (θ_D) of TiO₂, by ab initio calculations, which yields $h\nu_0 = k_B\theta_D = 67.4$ meV. Yelon and Movaghar²⁹ supposed that the optical phonons are the source of the excitation energy in this process. An additional substantiation of the nature of the conductivity in our films can be deduced from the value of σ_{00} , which provides valuable information on the charge transport mechanism. The relatively low value of σ_{00} ($2.17 \times 10^{-3} \Omega^{-1}/\text{cm}$) confirms that the transport is rather due to the hopping of carriers stimulated by optical phonons and to a lesser extent to the transport above the mobility edge.³¹ Therefore, the value of σ_{00} is again consistent with the picture proposed by Yelon and Movaghar.²⁹

As the temperature decreases ($T < \theta_D/2$), the process involves only a single polaron. Unlike this, in the high temperature range, $T > \theta_D/2$ (in our case, $T > 391$ K), the polaron motion predominates by thermal-activated jumps between neighboring sites, each accompanied by multiple-phonon emission and absorption.

Within the phonon-assisted hopping, two different types of conductivity can be distinguished. If there is a sufficiently strong electron–phonon interaction, small polarons are formed, and the electrical conduction occurs by the hopping of small polarons between the ions of low and high valence states of the transition metal ions.^{20,32} We have recently reported that the conduction mechanism in the undoped and low Fe-doped TiO₂ polycrystalline films can be described by small polaron hopping (SPH) for $T > \theta_D/2$. On the other hand, if the strength of the electron–phonon interaction is sufficiently weak, no small polaron can be formed.³³ In such a case, one can expect a different temperature dependent of conductivity as explained below. In the present films, the fit with the multiphonon-assisted hopping (MPH) model is better than the SPH fit.³⁴ When we have tried to fit to our data utilizing the SPH fit, we have obtained unrealistic physical parameters compared with previous work.²⁰ This may be related to the much different iron content in the TiO₂ films under study or to the different structures (here amorphous, while previous polycrystalline²⁰). Therefore, we had to apply the MPH conduction model to the conductivity data of the present films. We consider here that no small polaron can be formed, a hypothesis further supported by the fact that T_{MN} does not equal $\theta_D/2$. Kemeny and Rosenberg³⁴ reported that the SPH conduction can also lead to Eq. (3), in which case T_{MN} equals $\theta_D/2$. In our situation, therefore,

we can rule out the SPH conduction contribution to carrier transport. We were able to give an excellent account of our data in terms of the MPH with weak carrier–phonon coupling, as discussed below. If the transport proceeds via multiphonon tunneling of localized carriers with weak coupling, then the hopping rate (Γ) can be written as^{33,35}:

$$\Gamma = C \exp(-\gamma p) \left[\frac{k_B T}{h\nu_0} \right]^p, \quad (5)$$

while the conductivity is expressed as^{33,35}:

$$\sigma = \frac{n_c e^2 R^2 \Gamma}{6 k_B T}. \quad (6)$$

In the Eqs. (5) and (6), $C \sim \nu_0$, $\gamma = \ln(\Delta/E_M) - 1$, R is the hopping distance, $n_c = N(E_F)k_B T$. Here, $N(E_F)$ is the density of states at Fermi level, E_F . Unfortunately, an independent estimation of n_c and R is difficult, due to the lack of $N(E_F)$ values for these films. The parameter E_M (or γ) is a measure of the carrier–phonon coupling strength. A measure of the number of phonons participating in transport between hopping sites is also given by the ratio $p = \Delta/h\nu_0$, where Δ is the average site energy difference and $h\nu_0$ —the average energy of phonon modes coupled to the carriers. We may now write:

$$\sigma = A T^{p-1}. \quad (7)$$

One can expect that, theoretically, p should be an integer number since the MPH process involves the absorption and the emission of p phonons. However, if Δ , or ν_0 , are distributed around a certain value, the experimentally found p may have a finite distribution and its mean value will not be an integer and this is the case. Further analysis shows that the overall temperature-dependent conductivity in Fig. 7 is in good agreement with the above expression of the MPH conductivity. From the least squares straight line fits of Fig. 7, the values of p are obtained as 8.25, 14.20, and 14.50

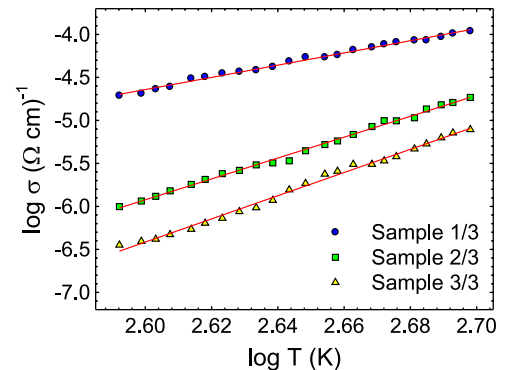


FIG. 7. Temperature dependence of the electrical conductivity plotted as $\log(\sigma)$ versus $\log T$ for the studied films. Solid lines are the best-fit lines with Eq. (7).

for Sample 1/3, Sample 2/3, and Sample 3/3, respectively. These values of p are comparable with those specific for the variety of disordered systems in which the MPH conduction was observed.^{36,37}

It is worth noting that in the viewpoint of hopping conduction, our data disagree with the single phonon-assisted variable range hopping (VRH) conduction mechanism because $h\nu_0$ is much smaller than Δ . The VRH requires the condition $p = \Delta/h\nu_0 < 1$. As indicated, the values of p estimated from the least squares straight line fits of Fig. 7 for the films are higher than 1, due to the fact that in the films, the MPH conduction dominates instead of a single phonon-assisted VRH conduction. Therefore, we conclude that the MPH conduction is the most probable conduction mechanism in the films. Finally, the origin of the MNR is attributed to the MPH for the investigated films.

IV. CONCLUSIONS

In this paper, we have obtained amorphous titania films, with increasing iron content, by RF sputtering. X-ray absorption (XANES and EXAFS) allowed the identification of local changes around Ti atoms with occurrence of more centrosymmetric phases than anatase; the same may be stipulated also from the XANES spectra of Fe K-edge, when a lower $3d-4p$ hybridization may explain the same decrease in the preedge peak. EXAFS performed at the Fe K-edge yielded the coexistence of two phases, one which is quite close to nanocrystalline magnetite and the other which is highly amorphous.

The temperature-dependent conductivity measurements, as performed on Fe/TiO₂ amorphous films, allowed us to evidence the MNR at temperatures higher than half of the Debye temperature ($T > 390$ K). Calculations give the σ_{00} as $2.17 \times 10^{-3} \Omega^{-1}/\text{cm}$ and the T_{MN} as approximately 980 K. It has been shown that the MNR can be described through the use of the MPH conduction model in the investigated films.

ACKNOWLEDGMENTS

This work was supported by CNCISIS Contract PCCE-ID_76/2010. Petronela Rambu and Daniel Florea acknowledge the financial support from the Romanian programs POS-DRU/89/1.5/S/49944 and POSDRU/CPP 107/DMI 1.5/S/78342, respectively.

REFERENCES

1. X. Quan, Q. Zhao, H. Tan, X. Sang, F. Wang, and Y. Dai: Comparative study of lanthanide oxide doped titanium dioxide photocatalysts prepared by coprecipitation and sol-gel process. *Mater. Chem. Phys.* **114**, 90 (2009).
2. Z.-M. Seeley, A. Bandyopadhyay, and S. Bose: Titanium dioxide thin films for high temperature gas sensors. *Thin Solid Films* **519**, 434 (2010).
3. D. Mardare, N. Iftimie, M. Crisan, M. Raileanu, A. Yildiz, T. Coman, K. Pomoni, and A. Vomvas: Electrical conduction mechanism and gas sensing properties of Pd-doped TiO₂ films. *J. Non-Cryst. Solids* **357**, 1774 (2011).
4. W. Jarembon, S. Pimanpang, S. Maensiri, E. Swatsitang, and V. Amornkitbamrung: Optimization of titanium dioxide film prepared by electrophoretic deposition for dye-sensitized solar cell application. *Thin Solid Films* **517**, 4663 (2009).
5. C. Euvananont, C. Junin, K. Inpor, P. Limthongkul, and C. Thanachayanont: TiO₂ optical coating layers for self-cleaning applications. *Ceram. Int.* **34**, 1067 (2008).
6. Y. Matsumoto, M. Murakami, T. Shono, T. Hasegawa, T. Fukumura, M. Kawasaki, P. Ahmet, T. Chikyow, S. Koshihara, and H. Koinuma: Room-temperature ferromagnetism in transparent transition metal-doped titanium dioxide. *Science* **291**, 854 (2001).
7. A.-P. Singh, S. Kumari, R. Shrivastav, S. Dass, and V.-R. Satsangi: Iron doped nanostructured TiO₂ for photoelectrochemical generation of hydrogen. *Int. J. Hydrogen Energy* **33**, 5363 (2008).
8. L. Fan, J. Dongmei, L. Yan, and M. Xueming: Magnetism of Fe-doped TiO₂ milled in different milling atmospheres. *Physica B* **403**, 2193 (2008).
9. D. Mardare, F. Iacomi, and D. Luca: Substrate and Fe-doping effects on the hydrophilic properties of TiO₂ thin films. *Thin Solid Films* **515**, 6474 (2007).
10. S.J. Gurman: Interpretation of EXAFS data. *J. Synchrotron Radiat.* **2**, 56 (1995).
11. J. Strunk, W.-C. Vining, and A.-T. Bell: A study of oxygen vacancy formation and annihilation in submonolayer coverages of TiO₂ dispersed on MCM-48. *J. Phys. Chem. C* **114**, 16937 (2010).
12. F. Farges, G.E. Brown, Jr., and J.J. Rehr: Ti K-edge XANES studies of Ti coordination and disorder in oxide compounds: Comparison between theory and experiment. *Phys. Rev. B* **56**, 1809 (1997).
13. C.M. Teodorescu, J.M. Esteve, M. Womes, A. El Afif, R.C. Karnatak, A.M. Flank, and P. Lagarde: Sodium 1s photoabsorption spectra of Na and NaF clusters deposited in rare gas matrices. *J. Electron. Spectrosc. Relat. Phenom.* **106**, 233 (2000).
14. C.M. Teodorescu, A. El Afif, J.M. Esteve, and R.C. Karnatak: Na 1s excitations in vapor and solid sodium halides. *Phys. Rev. B* **63**, 233106 (2001).
15. F. de Groot, G. Vankó, and P. Glatzel: The 1s x-ray absorption pre-edge structures in transition metal oxides. *J. Phys. Condens. Matter* **21**, 104207 (2009).
16. S. Matsuo, N. Sakaguchi, and H. Wakita: Pre-edge features of Ti K-edge x-ray absorption near-edge structure for the local structure of sol-gel titanium oxides. *Anal. Sci.* **21**, 805 (2005).
17. S. Sakurai, S. Sasaki, M. Okube, H. Ohara, and T. Toyoda: Cation distribution and valence state in Mn–Zn ferrite examined by synchrotron x-rays. *Physica B* **403**, 3589 (2008).
18. C. Dragoi, N.G. Gheorghe, G.A. Lungu, L. Trupina, A.G. Ibanescu, and C.M. Teodorescu: X-ray photoelectron spectroscopy of pulsed laser deposited Pb(Zr, Ti)O_{3-δ}. *Phys. Status Solidi A* **209**, 1049 (2012).
19. N.G. Gheorghe, M.A. Husanu, G.A. Lungu, R.M. Costescu, D. Macovei, D.G. Popescu, and C.M. Teodorescu: Magnetism and atomic structure in Fe/Si(001) interfaces. *Dig. J. Nanomater. Bios.* (2012, accepted).
20. A. Yildiz, F. Iacomi, and D. Mardare: Polaron transport in TiO₂ thin films. *J. Appl. Phys.* **108**(8), 083701 (2010).
21. D. Mardare and G.I. Rusu: Electrical conduction mechanism in polycrystalline titanium oxide thin films. *J. Non-Cryst. Solids* **356** (28–30), 1395 (2010).
22. W. Meyer and H. Neldel: Relation between the energy constant and the quantity constant in the conductivity–temperature formula of oxide semiconductors. *Z. Tech. Phys.* **12**, 588 (1937).

23. T.J. Coutts and N.M. Pearsall: Meyer–Neldel rule in solar cells. *Appl. Phys. Lett.* **44**(1), 134 (1984).
24. D.L. Stabler and C.R. Wronski: Optically induced conductivity changes in discharge-produced hydrogenated amorphous silicon. *J. Appl. Phys.* **51**(6), 3262 (1980).
25. B. Rosenberg, B.B. Bhowmik, H.C. Harder, and E. Postow: Pre-exponential factor in semiconducting organic substances. *J. Chem. Phys.* **49**(9), 4108 (1968).
26. K. Shimakawa and F. Abdel-Wahab: The Meyer–Neldel rule in chalcogenide glasses. *Appl. Phys. Lett.* **70**(5), 652 (1997).
27. R.S. Crandall: Defect relaxation in amorphous silicon: Stretched exponentials, the Meyer–Neldel rule, and the Staebler–Wronski effect. *Phys. Rev. B* **43**(5), 4057 (1991).
28. B.G. Yoon, C. Lee, and J. Jang: Effect of the statistical shift on the anomalous conductivities of n-type hydrogenated amorphous silicon. *J. Appl. Phys.* **60**(2), 673 (1986).
29. A. Yelon and B. Movaghar: The Meyer–Neldel conductivity prefactor for chalcogenide glasses. *Appl. Phys. Lett.* **71**(24), 3549 (1997).
30. X.J. Han, L. Bergqvist, P.H. Dederichs, H. Müller-Krumbhaar, J.K. Christie, S. Scandolo, and P. Tangney: Polarizable interatomic force field for TiO₂ parametrized using density functional theory. *Phys. Rev. B* **81**(13), 134108 (2010).
31. N.F. Mott: Conduction in glasses containing transition metal ions. *J. Non-Cryst. Solids* **1**(1), 1 (1968).
32. D. Emin and T. Holstein: Adiabatic theory of an electron in a deformable continuum. *Phys. Rev. Lett.* **36**(6), 323 (1976).
33. D. Emin: Phonon-assisted transition rates I. Optical-phonon-assisted hopping in solids. *Adv. Phys.* **24**(3), 305 (1975).
34. G. Kemeny and B. Rosenberg: Small polarons in organic and biological semiconductors. *J. Chem. Phys.* **53**(9), 3549 (1970).
35. N. Robertson and L. Friedman: Non-radiative transitions. *Philos. Mag.* **33**(5), 753 (1976).
36. K. Shimakawa: Phonon-assisted transition rates I. Optical-phonon-assisted hopping in solids. *Philos. Mag. B* **60**(3), 377 (1989).
37. H. Sakata, K. Sega, and B.K. Chaudhuri: Multiphonon tunneling conduction in vanadium-cobalt-tellurite glasses. *Phys. Rev. B* **60**(5), 3230 (1991).